

See discussions, stats, and author profiles for this publication at: <https://www.researchgate.net/publication/231232097>

Fabrication, In-Depth Characterization, and Formation Mechanism of Crystalline Porous Birnessite MnO₂ Film with Amorphous Bottom Layers by Hydrothermal Method

ARTICLE in CRYSTAL GROWTH & DESIGN · NOVEMBER 2008

Impact Factor: 4.89 · DOI: 10.1021/cg800312u

CITATIONS

42

READS

32

7 AUTHORS, INCLUDING:



De Yan

Lanzhou University

48 PUBLICATIONS 934 CITATIONS

SEE PROFILE



Peng X Yan

Lanzhou University

177 PUBLICATIONS 2,298 CITATIONS

SEE PROFILE



Shuang Cheng

South China University of Technology

24 PUBLICATIONS 754 CITATIONS

SEE PROFILE



Ren Fu Zhuo

Lanzhou University

30 PUBLICATIONS 738 CITATIONS

SEE PROFILE

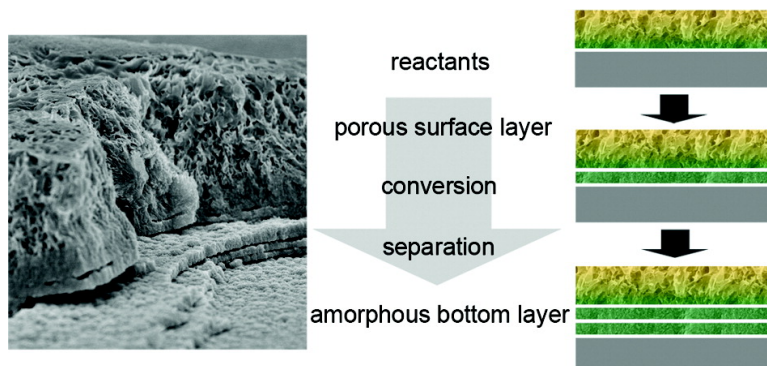
Article

Fabrication, In-Depth Characterization, and Formation Mechanism of Crystalline Porous Birnessite MnO Film with Amorphous Bottom Layers by Hydrothermal Method

De Yan, Pengxun Yan, Shuang Cheng, Jiangtao Chen,
Renfu Zhuo, Juanjuan Feng, and Guang'an Zhang

Cryst. Growth Des., **2009**, 9 (1), 218-222 • DOI: 10.1021/cg800312u • Publication Date (Web): 20 November 2008

Downloaded from <http://pubs.acs.org> on January 10, 2009



More About This Article

Additional resources and features associated with this article are available within the HTML version:

- Supporting Information
- Access to high resolution figures
- Links to articles and content related to this article
- Copyright permission to reproduce figures and/or text from this article

[View the Full Text HTML](#)



ACS Publications
High quality. High impact.

Fabrication, In-Depth Characterization, and Formation Mechanism of Crystalline Porous Birnessite MnO_2 Film with Amorphous Bottom Layers by Hydrothermal Method

De Yan,[†] Pengxun Yan,^{*,†,‡} Shuang Cheng,[†] Jiangtao Chen,[†] Renfu Zhuo,[†] Juanjuan Feng,[†] and Guang'an Zhang[†]

School of Physical Science and Technology, Lanzhou University, and Key Laboratory of Solid Lubrication, Institute of Chemistry and Physics, Chinese Academy of Science, Lanzhou 730000, China

Received March 24, 2008; Revised Manuscript Received May 24, 2008

ABSTRACT: Hydrated porous birnessite MnO_2 films were prepared on Si substrates and characterized in-depth by field emission scanning electron microscopy (FESEM), X-ray diffraction (XRD), transmission electron microscopy (TEM), selected area electron diffraction (SAED), X-ray photoelectron spectroscopy (XPS), and Fourier transform infrared spectroscopy (FT-IR). The as-prepared film is composed of a well-crystallized porous surface layer and one or more amorphous bottom layers. The morphology and structure of the film can be understood by the combined action of internal stress and conversion of the porous surface layer. The dynamic process of formation and conversion in the growth of porous surface layer is pointed out, which shows the transformation of reactants to amorphous bottom layers via the formation and conversion process of the porous surface layer. This result is of significant importance for increasing the utilization ratio of materials and for understanding basic physical and chemical processes of manganese oxide film growth under hydrothermal conditions.

1. Introduction

In recent years, the electrochemical capacitor has aroused great attention because of its high energy storage ability, high power output, and high cycle capacity, which has great potential applications in electric vehicles, power sources, and electronic devices.¹ There are mainly two types of capacitors: electric double-layer capacitance (e.g., graphite) and pseudocapacitance (e.g., transition metal oxides, such as hydrous RuO_2 , CoO_x , and MnO_2). The hydrous form of ruthenium oxide ($\text{RuO}_2 \cdot x\text{H}_2\text{O}$) presents a very high specific capacitance of 720 F/g, when measured with a 2 mV/s scan rate in sulfuric acid electrolyte.² CoO_x also exhibits excellent supercapacitance of about 750 F/g,³ and it was also used in more than 90% of lithium batteries manufactured.⁴ However, RuO_2 and CoO_x can not be widely used because of their high cost and toxicity. Therefore, manganese oxides are the most promising supercapacitor materials due to their high performance, low cost, and environmental friendliness.

Great attention has been focused on manganese oxide films in recent years to make them suitable for large-scale commercial production. Various approaches have been used to fabricate manganese oxide films, such as electrochemical deposition,^{5–7} sol–gel synthesis,^{8–11} and combination of physical vapor deposition (PVD) and electrochemical methods.^{12,13} Pang et al.¹⁴ reported the sol–gel-derived MnO_2 film exhibited a specific capacitance value as high as 698 F/g at a potential window of 0.9 V. However, films obtained by this method were often amorphous and contaminated with organic impurities.¹⁵ Wu¹⁶ prepared manganese oxide nanowire structure on nickel foils by an electrochemical route, and a specific capacitance of 350 F/g was obtained for discharge at 0.1 mA cm^{-2} . However, there is a great challenge encountered in the fabrication of electrochemically synthesized manganese oxide films. Larger oxidizing

current density results in more hydrated sites and thus can increase the specific capacitance,¹⁷ but the specific surface area of the film decreases at the same time and so plenty of material is wasted. The hydration and specific surface area are of opposing trends.¹⁸ Most papers have concentrated on the performance of manganese oxide films, and works focused on the mechanism study and in-depth characterization are rarely seen in the literature. Therefore, a comprehensive understanding of the structure and formation mechanism is urgently needed. Of course, developing new synthetic routes is another choice.

Here we report preparation of porous hydrated birnessite MnO_2 films on Si substrates by a simple hydrothermal route. In-depth structure characterization and study on formation mechanism were carried out. Internal stress and conversion of the porous surface layer are believed to play an important role in the growth of the as-prepared MnO_2 film. The dynamic process of formation and conversion in the growth of the porous surface layer is also pointed out, which is of significant importance for increasing the utilization ratio of materials and the understanding of basic physical and chemical process of manganese oxide film growth in hydrothermal conditions. To the best of our knowledge, the mechanism we propose has not been previously reported.

2. Experimental Section

KMnO_4 (200 mg, analytical grade, >99.5%) was dissolved in deionized water under magnetic stirring, with the total volume of the solution 30 mL. Si substrates [single crystal, (100) orientation] were ultrasonically rinsed in absolute ethanol for about 10 min. Then the solution and the Si substrate were transferred into a Teflon [poly(tetrafluoroethylene), PTFE]-lined autoclave with a capacity of 43.5 mL, tightly sealed, oven-heated at 150 °C for 72 h, and then cooled down to room temperature naturally. The product was repeatedly washed with deionized water and dried at room temperature to obtain the final product. Manganese oxide films on a 1 cm × 1 cm and a 2 cm × 2 cm Si substrate were prepared.

The samples were characterized by X-ray diffraction (XRD) on a Rigaku D/Max-2400 and a Philips X' Pert Pro Diffractometer using $\text{Cu K}\alpha_1$ irradiation ($\lambda = 1.54056 \text{ \AA}$). Transmission electron microscopy (TEM) and selected area electron diffraction (SAED) were carried out

* Corresponding author: School of Physical Science and Technology, Lanzhou University, Lanzhou City, Gansu Province, China 730000. Tel 86-931-8912719; fax 86-931-8913554; e-mail pxyan@lzu.edu.cn.

[†] Lanzhou University.

[‡] Chinese Academy of Science.

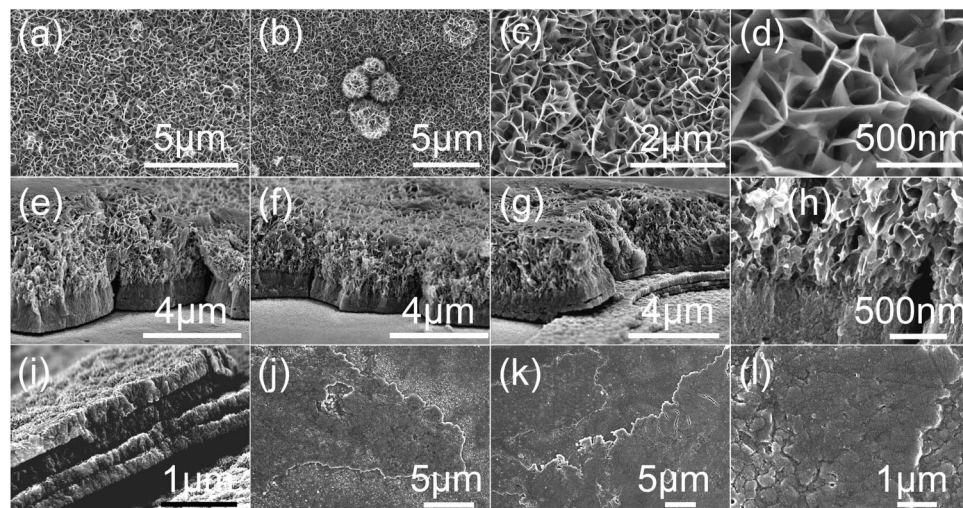


Figure 1. FESEM images of the film prepared on a 1 cm × 1 cm Si substrate. (a–d) Top view of porous surface layer of the film. (e–h) Side view of the film. (i–l) Side and top view of the bottom layers, with the porous surface layer scraped off.

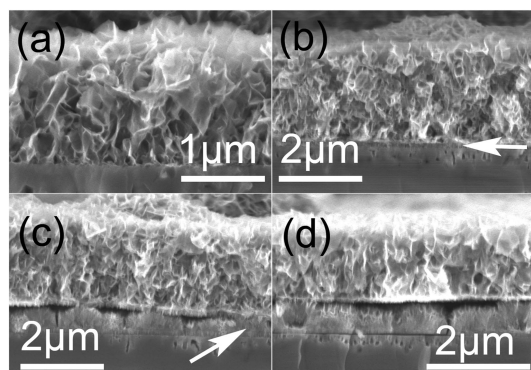


Figure 2. FESEM images of the film prepared on a 2 cm × 2 cm Si substrate.

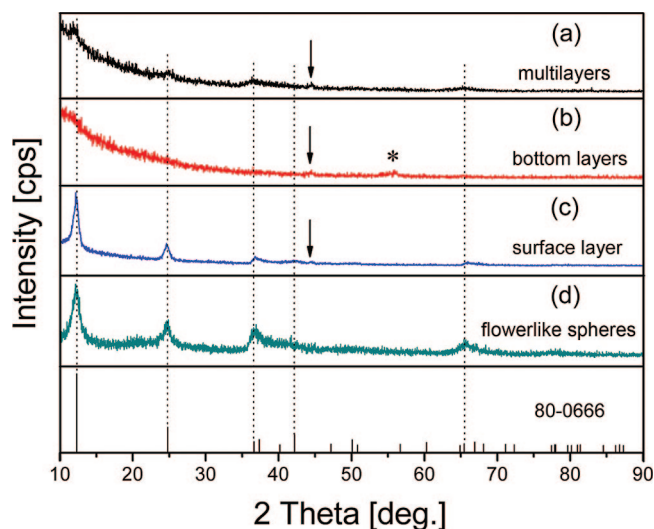


Figure 3. (a, b) XRD pattern of the sample in Figure 1, (a) with and (b) without the surface layer. (c) XRD pattern of the sample shown in Figure 2, mainly the porous surface layer. (d) XRD pattern of the flowerlike spheres from the mother solution.

on a Hitachi H-600 transmission electron microscope operated at 100 kV. Field emission scanning electron microscopy (FESEM) observation was performed on a Hitachi S-4800 and a JSM-6701F field emission scanning electron microscope. The film surface was analyzed

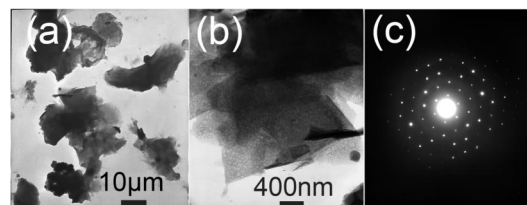


Figure 4. (a, b) TEM images of the porous surface layer of the film shown in Figure 1. (c) SAED pattern taken from panel b.

on a PHI-5702 X-ray photoelectron spectroscopy (XPS) operating with monochromatic Al K α irradiation at pass energy of 29.4 eV. Fourier transform infrared (FT-IR, Bruker IFS66V/S) spectra were recorded for the flakes of samples pressed with KBr powder, which was dried at 70 °C to eliminate the effect of water molecules, and the influence of substrate was deducted.

3. Results and Discussion

The morphology of the manganese oxide film prepared on a 1 cm × 1 cm Si substrate was investigated by FESEM. Figure 1 shows the top view (panels a–d) and side view (panels e–h) of the film. It clearly shows that the film is composed of a porous surface layer about 3–4 μm thick and several bottom layers about 200–300 nm thick each. The porous surface layer of the film consists of a large quantity of nanosheets with thickness of about 3–5 nm, as shown in Figure 1d. Figure 1h clearly shows the transformation area at the root of the porous surface layer. Figure 1i shows the side view of typical bottom layers and some veinlike structures on their surface can be seen. Top view of the bottom layers is shown in Figure 1j–l with the porous surface layer scraped off. It can be seen that the surface of the bottom layers is full of fissures, which is consistent with Figure 1e–g. There are also several porous flowerlike spheres still remaining on the film surface even after repeated washing with deionized water (Figure 1b). The precipitates in mother solution are all such porous flowerlike spheres composed of single-crystalline nanosheets, which was previously reported by our group.¹⁹

Figure 2 shows the side view of the manganese oxide film prepared on a 2 cm × 2 cm Si substrate. The morphology of the film does not show an obvious change, except that the thickness of the porous layer decreases to about 2 μm and the bottom layer increases to about 600 nm. No bottom layer can

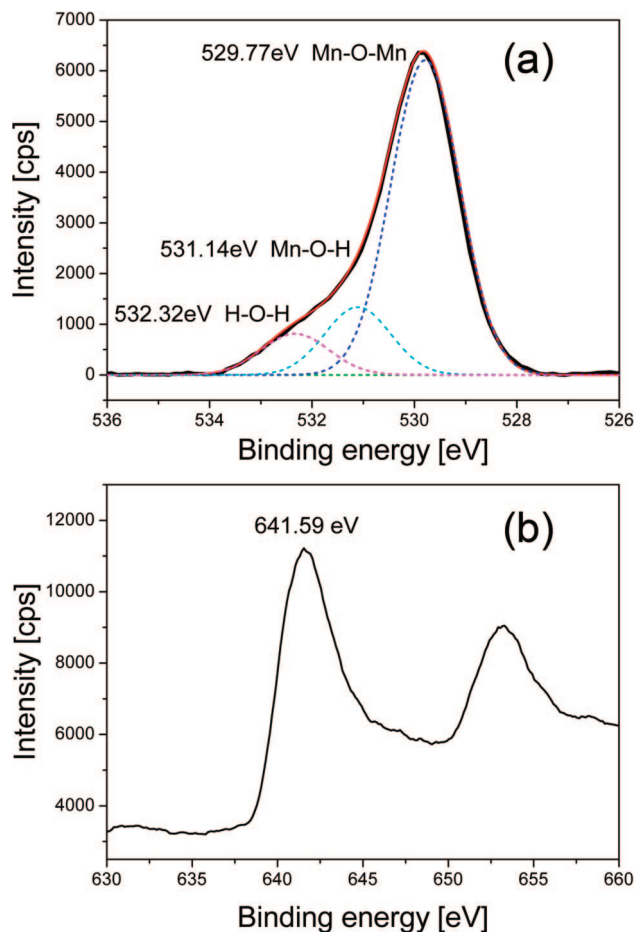


Figure 5. XPS of the porous surface layer of the sample shown in Figure 1. (a) O 1s peak; (b) Mn 2p_{3/2} peak.

be found in Figure 2a. A thin dense layer of about 170 nm appears in Figure 2b at the root of the surface layer. Figure 2c indicates the bottom layer is not completely separated from the surface layer, and Figure 2d shows the area where the separation is complete. Although these images were taken from different regions of the film, they may represent different stages of the growth process according to their different thicknesses.

XRD patterns of the as-prepared films and the flowerlike spheres from the mother solution are shown in Figure 3. Obviously, panels a, c, and d show the same structure. All of the peaks can be indexed to hexagonal birnessite MnO₂ (JPCDS 86-0666), which consists of 2D edge-shared MnO₆ octahedra layers with K⁺ cations and water molecules in the interlayer space.¹⁹ The peak indicated by the arrows is from the XRD equipment itself. Figure 3b indicates that the bottom layers are almost amorphous except for the weak wide peak indicated by the asterisk, which probably comes from poorly crystallized γ -Mn₂O₃ (JPCDS 24-0734). The composition of the bottom layers will be discussed later in this paper on the basis of FT-IR spectra.

The porous surface layer that was scraped off from the sample shown in Figure 1 was ultrasonically dispersed in ethanol and subjected to TEM analysis. Figure 4a,b shows that the porous surface is composed of thin nanosheets. The SAED pattern (Figure 4c) is taken from Figure 4b, which clearly reveals that the nanosheet is single-crystalline.

The porous surface layer of the manganese oxide film was studied by XPS to obtain further structural information. The O 1s spectrum was deconvoluted into three components as shown

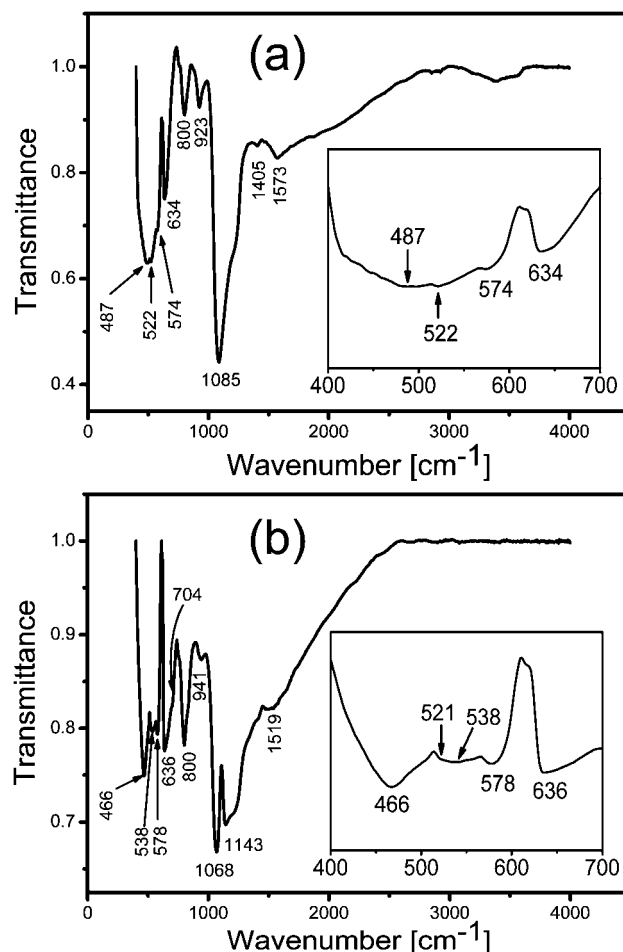


Figure 6. FT-IR spectra of the manganese oxide film shown in Figure 1: (a) porous surface layer with amorphous bottom layers; (b) amorphous bottom layers only. (Insets) Partially enlarged spectra from 400 to 700 cm⁻¹.

in Figure 5a: the anhydrous compounds (Mn–O–Mn) peak at 529.77 eV, the hydrated manganese (Mn–O–H) peak at 531.14 eV, and the water molecule (H–O–H) peak at 532.32 eV. This is in good agreement with literature values of 529.3–530.3 eV for oxide, 530.5–531.5 eV for hydroxide, and 531.8–532.8 eV for water.^{1,12,20} The relative contents of Mn–O–Mn, Mn–O–H, and H–O–H are about 75%, 15%, and 10%, respectively. It is difficult to determine the valence of Mn ion from only the Mn 2p_{3/2} peak.²⁰ The observed Mn 2p_{3/2} peak found at 641.59 eV is consistent with its assignment as Mn⁴⁺, and this was confirmed by XRD analysis. Since the hydrated manganese oxide is solely responsible for the film's capacitance,¹² the as-prepared MnO₂ film may have great potential applications as supercapacitors.

Since the bottom layers are amorphous as shown by XRD analysis, FT-IR was utilized to further investigate their phase composition because it is sensitive to both crystalline materials with long-range order and amorphous materials with short-range order.²¹ Figure 6 shows the FT-IR spectra of the film shown in Figure 1, with (a) and without (b) the porous surface layer. The broad bands in Figure 6a at about 3400 and 1573 cm⁻¹ are caused by the stretching vibration of O–H bond and the bending vibration of H–O–H in water. By comparison with Figure 6b, it can be deduced that water molecules exist only in the porous surface layer. The strong peak at 800 cm⁻¹ can be attributed to the symmetric Si–O–Si vibration, and the peaks at 1143, 1085, and 1068 cm⁻¹ can be attributed to the

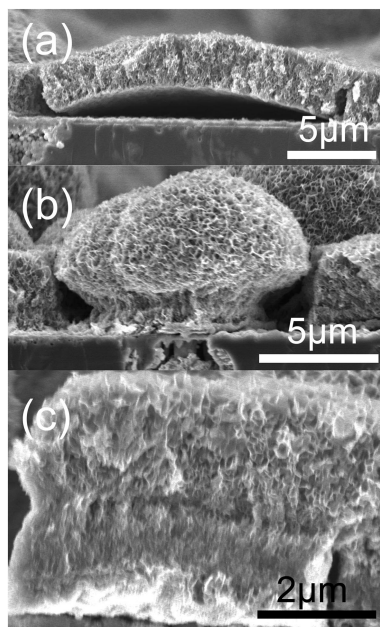


Figure 7. SEM images of the same sample as in Figure 2. (a) Curved film indicating the existence of internal stress. (b) Mushroomlike structure. (c) Separation of the first bottom layer with a boundary in the middle.

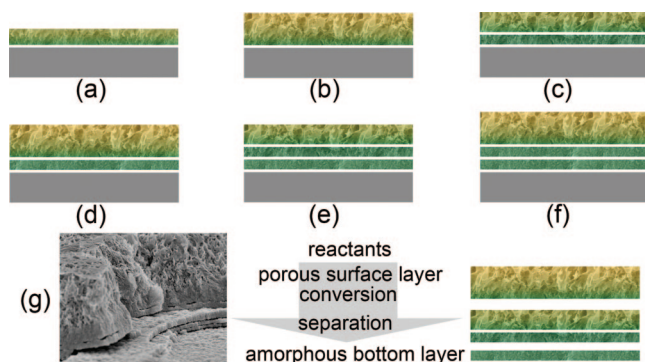


Figure 8. Schematic illustration of the film growth process. (a) First, a thin porous surface layer is grown on the Si substrate. (b) Internal stress increases and the root region of the porous layer converts to amorphous status at the same time the film thickness is increasing. (c) Separation of the first bottom layer from surface layer; internal stress is released at the same time. (d–f) Formation of the second bottom layer (d and f are mainly of the same case as b; e is mainly of the same case as c). (g) Dynamic process that shows the transformation of reactants to amorphous bottom layers via the formation and conversion process of the porous surface layer.

asymmetric vibrations of Si–O–Si.^{22,23} The bands at 923 and 941 cm^{−1} are assigned to the stretching vibration of Si–OH.^{23,24} It is also reported that the peaks at 923 and 941 cm^{−1} can be caused by hydrogen-bonded -OH deformation vibration in manganese hydroxide,²⁵ and the peaks at 1085 and 1068 cm^{−1} can be caused by -OH bending modes.^{25–28} The appearance of 522 and 1085 cm^{−1} peaks and of 521 and 1068 cm^{−1} peaks in Figure 6 indicate the appearance of manganite (γ-MnOOH) in the amorphous bottom layers.^{21,29} The bands at 574 and 578 cm^{−1} in Figure 6a,b may be caused by the antisymmetry stretching mode of MnO₆ octahedra in γ-MnO₂.^{21,29–31} γ-Mn₃O₄ may also appear in the bottom layers due to the bands at 522 and 634 cm^{−1} in Figure 6a and at 538 and 636 cm^{−1} in Figure 6b.^{32–34} The bands at 487 and 522 cm^{−1} in Figure 6a indicate the formation of birnessite MnO₂, which is in accord with XRD

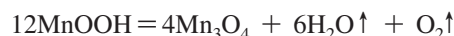
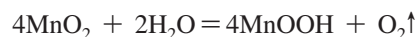
analysis.^{21,35} α-MnO₂ may also exist in bottom layers of the manganese oxide film according to the bands at 466, 538, and 578 cm^{−1} and the shoulder peak at 704 cm^{−1} (Figure 6b).^{27,36} It is deduced that α-MnO₂ should also be found in Figure 6a, but we cannot confirm the appearance of α-MnO₂ due to the absence of the peak around 704 cm^{−1}. The reason may be that the 704 cm^{−1} peak is too weak to be detected. Therefore, the bottom layers of the manganese dioxide film may consist of γ-MnOOH, γ-Mn₃O₄, γ-MnO₂, α-MnO₂, and -OH bonded with Mn and Si ions.

Figure 7 shows some side-view images of the same sample shown in Figure 2, which are helpful to understand the formation mechanism of the film. The curved film shown in Figure 7a indicates the existence of internal stress in the porous surface layer. Figure 7b shows the dendritic growth of the porous surface layer. The top of the mushroomlike structure grows much bigger than the bottom. Figure 7c shows the image when the first bottom layer is separating from the surface layer, with an obvious boundary in the middle.

A possible mechanism is proposed to understand the formation of the MnO₂ film with amorphous bottom layers, and the schematic illustration of this mechanism is shown in Figure 8. The main driving force is believed to be the combined action of internal stress and conversion of the porous surface layer. First, a thin porous film of birnessite MnO₂ is formed on the Si substrate (Figure 8a) due to the decomposition of KMnO₄ in water, which can be formulated as



The internal stress of the porous film was generated and increases as the film thickness increases (Figure 8b). The generation of internal stress is due to the dendritic growth of the film (Figure 7b). The branches in the top of the porous film are more dense than in the bottom region, so the internal stress that makes the film bend in Figure 7a is actually the repelling force among the dense branches on top of the porous layer. Thus the formation of mushroomlike morphology (Figure 7b) is easy to understand. As the porous layer grows thicker and thicker, the root region of the porous layer is isolated from the mother solution by the top region of the porous layer and the substrate. Under the isolated local conditions and the self-generated pressure in the autoclave, a series of complicated reversible reactions may take place at the root region of the porous surface layer, which could result in the amorphous nature of the bottom layers (Figure 8b). The reactions that take place may include the following:



Figures 1 and 2 show that the porous surface layer often has a thin amorphous part in the root region, so the amorphous part does not immediately separate from the surface layer after its formation. The separation (Figure 8c) occurs only when the thickness of the amorphous part reaches a certain value; in other words, the separation occurs only when the internal stress of the top layer reaches a certain value. It needs to be pointed out that the stress generated on the interface between the amorphous and crystalline parts of the top layer may also make certain contributions to the separation. Formation of the subsequent bottom layers (Figure 8d–f) is mainly of the same case as the first bottom layer. Thus it is seen from Figure 1g,i that the thickness of the bottom layers is mainly the same. The thickness

increase of the porous surface layer may slow down after the amorphous root region develops. While the porous surface layer is growing on the exposed surface, the amorphous bottom layer grows as well due to the conversion (via the reactions shown above) at the base of the top layer. Figure 8g shows the dynamic process, which clearly reveals the transformation of reactants to the amorphous bottom layers via the formation and conversion process of the porous surface layer.

Formation of the porous feature of the surface layer may be attributed to the coulombic interaction between K^+ cations, birnessite MnO_2 nanosheets with negative surface charge, and polar H_2O molecules, according to our previous work.¹⁹ The veinlike structure on the surface of bottom layers shown in Figure 1i may be the remaining porous crystalline birnessite MnO_2 after separation. The complicated reactions happening in the bottom part of the top layer may go on after separation, and that is why the veinlike structure is not found in Figure 1j–l. Moreover, the surface of Si substrate is oxidized to SiO_2 as indicated by the cavities in Si substrate (Figures 2b and 7b). It needs to be pointed out that the bent shape of the film shown in Figure 7a should not appear according to the above discussion. Its appearance was caused by the release of internal stress induced by the strike of outside force during the sample preparation for FESEM observation. Moreover, larger substrate results in thicker bottom layers (compare Figures 1 and 2), because larger substrate makes the separation more difficult according to the above discussion. Larger substrate also easily causes nonuniformity and deficiencies in the film (Figure 7b,c) because of the nonuniform release of internal stress. Therefore, the observed morphology and structure of the as-prepared MnO_2 film can be understood according to the above proposed mechanism. However, the exact mechanism is still unknown and further investigation needs to be carried out.

It needs to be pointed out that this mechanism may also be used to explain the formation of films with amorphous layers prepared by electrochemical methods after minor changes. The formation and conversion dynamic process of the hydrated porous surface layer growth is of significant importance for increasing the utilization ratio of materials. According to this mechanism, the highest utilization ratio of materials appears just before conversion of the porous surface layer occurs. Therefore, delaying or eliminating the conversion of the porous surface layer is of great importance for increasing the utilization ratio of materials.

4. Conclusion

Birnessite MnO_2 films were prepared on Si substrates by a very simple and facile hydrothermal method at 150 °C, with $KMnO_4$ and deionized water as reactants. The as-prepared film has a porous surface layer and generally one or more bottom layers. The porous surface layer is identified as hydrated birnessite MnO_2 , with hydrated content ($Mn-O-H$) of about 15%. Since the porous layer is solely responsible for the supercapacitance of manganese oxide,¹² the as-prepared films may be used as supercapacitors. The amorphous bottom layers may consist of γ - $MnOOH$, γ - Mn_3O_4 , γ - MnO_2 , α - MnO_2 , and $-OH$ bonded with Mn and Si ions. A mechanism was proposed to understand the formation of the as-prepared film. The main driving force responsible for the formation of amorphous bottom layers is attributed to internal stress and conversion of the porous surface layer. The formation and conversion dynamic process in the growth process of the porous surface layer is pointed out. The highest utilization ratio of material appears at the time just before conversion of the porous layers

happens. Therefore, delaying or eliminating the conversion of the porous surface layer is of great importance for increasing the utilization ratio of materials. The growth mechanism is also of significant importance for promoting an understanding of basic physical and chemical processes of film growth under hydrothermal conditions.

Acknowledgment. This work was supported by funds from National Natural Science Foundation of China (Grant 60376039). We thank YouXiang Li from Instrument Analysis & Testing Center of Gansu Academy of Science for TEM instrument analysis.

References

- (1) Nagarajan, N.; Cheong, M.; Zhitomirsky, I. *Mater. Chem. Phys.* **2007**, *103*, 47–53.
- (2) Zheng, J. P.; Jow, T. R. *J. Electrochem. Soc.* **1995**, *142*, L6–L8.
- (3) Srinivasan, V.; Weidner, J. W. *J. Power Sources* **2002**, *108*, 15–20.
- (4) Amundsen, B.; Paulsen, J. *Adv. Mater.* **2001**, *13*, 943–956.
- (5) Therese, G. H. A.; Kamath, P. V. *Chem. Mater.* **2000**, *12*, 1195–1204.
- (6) Nakayama, M.; Konishi, S.; Tagashira, H.; Ogura, K. *Langmuir* **2005**, *21*, 354–359.
- (7) Wang, L. Z.; Omomo, Y.; Sakai, N.; Fukuda, K.; Nakai, I.; Ebina, Y.; Takada, K.; Watanabe, M.; Sasaki, T. *Chem. Mater.* **2003**, *15*, 2873–2878.
- (8) Long, J. W.; Young, A. L.; Rolison, D. R. *J. Electrochem. Soc.* **2003**, *150*, A1161–A1165.
- (9) Long, J. W.; Qadir, L. R.; Stroud, R. M.; Rolison, D. R. *J. Phys. Chem. B* **2001**, *105*, 8712–8717.
- (10) Segal, S. R.; Park, S. H.; Suib, S. L. *Chem. Mater.* **1997**, *9*, 98–104.
- (11) Ching, S.; Welch, E. J.; Hughes, S. M.; Bahadoor, A. B. F.; Suib, S. L. *Chem. Mater.* **2002**, *14*, 1292–1299.
- (12) Djurfors, B.; Broughton, J. N.; Brett, M. J.; Ivey, D. G. *Acta Mater.* **2005**, *53*, 957–965.
- (13) Djurfors, B.; Broughton, J. N.; Brett, M. J.; Ivey, D. G. *J. Mater. Sci.* **2003**, *38*, 4817–4830.
- (14) Pang, S. C.; Anderson, M. A.; Chapman, T. W. *J. Electrochem. Soc.* **2000**, *147*, 444–450.
- (15) Hu, C. C.; Tsou, T. W. *Electrochim. Acta* **2002**, *47*, 3523–3532.
- (16) Wu, M. S. *Appl. Phys. Lett.* **2005**, *87*, 153102–153104.
- (17) Chun, S. E.; Pyun, S. I.; Lee, G. J. *Electrochim. Acta* **2006**, *51*, 6479–6486.
- (18) Djurfors, B.; Broughton, J. N.; Brett, M. J.; Ivey, D. G. *J. Power Sources* **2006**, *156*, 741–747.
- (19) Yan, D.; Yan, P. X.; Yue, G. H.; Liu, J. Z.; Chang, J. B.; Yang, Q.; Qu, D. M.; Geng, Z. R.; Chen, J. T.; Zhang, G. A.; Zhuo, R. F. *Chem. Phys. Lett.* **2007**, *440*, 134–138.
- (20) Chigane, M.; Ishikawa, M. *J. Electrochem. Soc.* **2000**, *147*, 2246–2251.
- (21) Potter, R. M.; Rossman, G. R. *Am. Mineral.* **1979**, *64*, 1199–1218.
- (22) Drago, R. S.; Dias, S. C.; McGivray, J. M.; Mateus, A. L. M. L. *J. Phys. Chem. B* **1998**, *102*, 1508–1514.
- (23) Lin, J.; Siddiqui, J. A.; Ottenbrite, R. M. *Polym. Adv. Technol.* **2001**, *12*, 258–292.
- (24) Fonaseca, C. D.; Ozanam, F.; Chazalviel, J. N. *Surf. Sci.* **1996**, *365*, 1–14.
- (25) Feng, X. H.; Tan, W. F.; Liu, F.; Huang, Q. Y.; Liu, X. W. *Sci. China, Ser. D: Earth Sci.* **2005**, *48*, 1438–1451.
- (26) Zhang, W. X.; Yang, Z. H.; Liu, Y.; Tang, S. P.; Han, X. Z.; Chen, M. *J. Cryst. Growth* **2004**, *263*, 394–399.
- (27) Yang, R. Z.; Wang, Z. X.; Dai, L.; Chen, L. Q. *Mater. Chem. Phys.* **2005**, *93*, 149–153.
- (28) Navak, A. *Struct. Bonding (Berlin)* **1974**, *18*, 177–216.
- (29) Greene, A. C.; Madgwick, J. C. *Appl. Environ. Microbiol.* **1991**, *57*, 1114–1120.
- (30) Banov, B.; Momchilov, A.; Massot, M.; Julien, C. M. *Mater. Sci. Eng., B* **2003**, *100*, 87–92.
- (31) Julien, C. M.; Massot, M. *J. Power Sources* **2003**, *119–121*, 743–748.
- (32) Gibot, P.; Laffont, L. *J. Solid State Chem.* **2007**, *180*, 695–701.
- (33) Du, J.; Gao, Y. Q.; Chai, L. L.; Zou, G. F.; Li, Y.; Qian, Y. T. *Nanotechnology* **2006**, *17*, 4923–4928.
- (34) Ishii, M.; Nakahira, M. *Solid State Commun.* **1972**, *11*, 209–212.
- (35) Luo, J.; Zhang, Q. H.; Suib, S. L. *Inorg. Chem.* **2000**, *39*, 741–747.
- (36) Wang, H. E.; Qian, D.; Lu, Z. G.; Li, Y. K.; Cheng, R. J.; Li, Y. J. *J. Phys. Chem. Solids* **2007**, *68*, 1422–1427.